

UCSF

UC San Francisco Previously Published Works

Title

Comparison between 8- and 32-channel phased-array receive coils for in vivo hyperpolarized ¹³C imaging of the human brain

Permalink

<https://escholarship.org/uc/item/5w36q4d0>

Journal

Magnetic Resonance in Medicine, 82(2)

ISSN

0740-3194

Authors

Autry, Adam W
Gordon, Jeremy W
Carvajal, Lucas
[et al.](#)

Publication Date

2019-08-01

DOI

10.1002/mrm.27743

Peer reviewed



Published in final edited form as:

Magn Reson Med. 2019 August ; 82(2): 833–841. doi:10.1002/mrm.27743.

Comparison between 8- and 32-channel phased-array receive coils for *in vivo* hyperpolarized ^{13}C imaging of the human brain

Adam W Autry¹, Jeremy W Gordon¹, Lucas Carvajal¹, Azma Mareyam², Hsin-Yu Chen¹, Ilwoo Park³, Daniele Mammoli¹, Maryam Vareth^{1,4}, Susan M Chang⁵, Lawrence L Wald^{2,6,7}, Duan Xu¹, Daniel B Vigneron¹, Sarah J Nelson^{1,8}, and Yan Li^{1,*}

¹Department of Radiology and Biomedical Imaging, University of California San Francisco, San Francisco, USA,

²Athinoula A Martinos Center for Biomedical Imaging, Department of Radiology, Massachusetts General Hospital, Charlestown, Massachusetts, USA,

³Department of Radiology, Chonnam National University Medical School and Hospital, Gwangju, Korea,

⁴Berkeley Institute for Data Science (BIDS), University of California Berkeley, Berkeley, USA,

⁵Department of Neurological Surgery, University of California San Francisco, San Francisco, USA,

⁶Harvard Medical School, Boston, Massachusetts, USA,

⁷Harvard-MIT Health Sciences and Technology, MIT, Cambridge, Massachusetts, USA,

⁸Department of Bioengineering and Therapeutic Science, University of California San Francisco, San Francisco, USA

Abstract

Purpose: To compare the performance of an 8-channel surface coil/clamshell transmitter and 32-channel head array coil/birdcage transmitter for hyperpolarized ^{13}C brain metabolic imaging.

Methods: In order to determine the field homogeneity of the RF transmitters, B_1+ mapping was performed on an ethylene glycol head phantom and evaluated via the double angle method. Using a 3-D echo-planar imaging (EPI) sequence, coil sensitivity and noise-only phantom data were acquired with the 8- and 32-channel receiver arrays, and compared against data from the birdcage in transceiver mode. Multislice frequency-specific ^{13}C dynamic EPI was performed on a patient with a brain tumor for each hardware configuration following injection of hyperpolarized $[1-^{13}\text{C}]$ pyruvate. SNR was evaluated from pre-whitened phantom and temporally summed patient data after coil combination based on optimal weights.

Results: The birdcage transmitter produced more uniform B_1+ compared to the clamshell: 0.07 versus 0.12 (fractional error). Phantom experiments conducted with matched lateral housing separation demonstrated 8- versus 32-channel mean transceiver-normalized SNR performance: 0.91 versus 0.97 at the head center; 6.67 versus 2.08 on the sides; 0.66 versus 2.73 at the anterior;

*Corresponding author: Yan Li, Department of Radiology and Biomedical Imaging, University of California San Francisco, Ste 350, 185 Berry Street, San Francisco 94107, USA, yan.li@ucsf.edu.

and 0.67 versus 3.17 on the posterior aspect. While the 8-channel receiver array showed SNR benefits along lateral aspects, the 32-channel array exhibited greater coverage and a more uniform coil-combined profile. Temporally-summed, parameter-normalized patient data showed SNR_{mean, slice} ratios (8-channel/32-channel) ranging 0.5–2.00 from apical to central brain. White matter lactate-to-pyruvate ratios were conserved across hardware: 0.45±0.12 (8-channel) versus 0.43±0.14 (32-channel).

Conclusion: The 8- and 32-channel hardware configurations each have advantages in particular brain anatomy.

Keywords

hyperpolarized; carbon-13; 32-channel; phased-array; echo-planar imaging; brain

Introduction

Following the discovery of dissolution dynamic nuclear polarization (d-DNP) techniques (1), the field of hyperpolarized ¹³C imaging has enabled diverse applications for non-invasively probing real-time metabolism *in vivo* (2–4). In the context of clinical translation, validating the utility of these applications is key to understanding their potential diagnostic impact. While d-DNP affords appreciable signal enhancement via spin polarization, metabolites downstream of the substrate can fall within a low SNR regime, given their enzyme-mediated conversion, signal decay from T₁ and RF utilization, and label/molecule-dependent T₁-shortening effects. Such time-sensitive and unrecoverable magnetization in hyperpolarized experiments underscores the importance of RF hardware design that improves SNR by conforming to organ-specific demands.

Hyperpolarized ¹³C imaging of the human brain presents unique challenges. Initial clinical trials on patients with brain tumors (5,6) determined that hyperpolarized [1-¹³C]pyruvate crosses the blood-brain barrier and undergoes considerable metabolic conversion over the timescale of the experiment. Despite demonstrating feasibility using an 8-channel ¹³C bilateral surface coil array and clamshell transmit coil, Park *et al.* recognized the importance of adequate SNR for achieving clinically relevant spatial resolution, which is limited by the size and geometric shape of the brain (5,7). As the number of elements increases in a multi-channel phased-array receiver, the SNR is expected to improve to a limit at the center, however the ultimate SNR on the periphery requires additional elements with smaller diameter and greater sensitivity (8, 9). This is how a head array can yield comparable SNR to the 8-channel receiver at the center of the brain, while providing more homogeneous coil-combined profiles and increased potential for accelerating data acquisition via parallel imaging (10,11). Because actual hardware implementations can deviate from theoretical considerations, this study was designed to compare the performance of the 8-channel/clamshell coil configuration with a 32-channel ¹³C head array and birdcage transmit coil in phantom and patient experiments using variants of a frequency-specific echo-planar imaging (EPI) sequence (12).

Methods

Coil Configuration

All experiments were performed on a clinical 3T whole body scanner (MR 750; GE Healthcare, Waukesha, WI) equipped with 32-channel multi-nuclear imaging capability. Investigation centered around two custom-designed RF hardware configurations: 1) bilateral paddle coils that had a total of 8 elements with a clamshell transmit coil (Figure 1A,B) (7,13); and 2) a 32-channel head array coil with integrated birdcage transmit coil (Figure 1C,D)(14). Design of the paddle assemblies comprised 4 overlapping copper loops of dimension $5 \times 10 \text{ cm}^2$, which had been tuned and matched at 32.12 MHz for carbon. The clamshell transmitter consisted of a capacitively-coupled Helmholtz pair with resonant loops of approximately $30.5 \times 30.5 \text{ cm}^2$, housed in a hinged architecture that provided easy access for patients (13,15). This transmitter was actively detuned during reception using a reverse/forward bias of $-2.5/590 \text{ VDC}$ for an active pin trap on each loop. For the 32-channel array ($Q_{\text{unloaded}}/Q_{\text{loaded}} = 250/90$), elements of approximately 8–10 cm diameter were arranged on the housing according to hexagonal/pentagonal soccer ball geometry, with more elongated loops around the region encompassing the neck. Integrated into the head array assembly was a 16-rung low-pass birdcage transmit coil having a 30.5 cm diameter and 32 cm rung length. This transmitter was actively detuned during reception using a reverse/forward bias of $-2.0/300 \text{ VDC}$ for a pin diode trap constructed on every other rung. In both ^{13}C receiver arrays, a return loss (S_{11}) $< -17\text{dB}$ and transmission loss (S_{21}) $< -17 \text{ dB}$ were measured. In each case, dynamic disabling of carbon receive channels during RF transmission was accomplished via a pin diode trap, and proton frequencies for anatomical imaging were passively blocked with a second trap circuit. Table 1 summarizes these specifications and circuit schematics are shown in Supporting Information Figure S1.

Phantom Imaging

A head-shaped phantom containing unenriched ethylene glycol ($\text{HOCH}_2\text{CH}_2\text{OH}$, anhydrous, 99.8%, Sigma Aldrich, St. Louis, MO) doped with 17g/L (0.29 M) NaCl for loading was used to maintain *in vivo* hardware configurations and evaluate their performance over representative spatial regions (Figure 1E). Positioning of the transmitter and receiver assemblies was designed to maximize the quality of each acquisition, while preserving the ability for cross-platform comparison. In the case of the 8-channel/clamshell assembly, the phantom was placed on the integrated headrest with the paddle coils centered about the transmitter R-L isocenter and separated by 19cm ($8\text{ch}_{19\text{cm}}$) to mimic the 32-channel housing and 16.3cm ($8\text{ch}_{16.3\text{cm}}$) to match some *in vivo* experiments (Figure 1C). The 16.3cm separation was at the center of the curved 8-channel housing and equivalent to placing the paddles directly against the phantom with 15cm width. The phantom was landmarked at the transmitter R-L/S-I isocenter, which corresponded with anatomical features that could readily be referenced from proton images. The 32-channel receiver array was fixed relative to the birdcage transmitter, allowing the phantom to be inserted into the housing on a thin pad and landmarked in a similar manner. As a reference benchmark for normalizing SNR, the phantom was also scanned using only the birdcage coil in transceiver mode.

Proton T₂-weighted fast spin echo (FSE) images (TR/TE=4000/60ms, 26-cm FOV, 192×256 matrix, 5mm slice thickness and 2 NEX) of the phantom were acquired using the scanner body coil. A ¹³C FID sequence (GE Healthcare) provided the ability to determine the appropriate center frequency and calibrate power (TG) with a non-slice selective 90° or 180° RF pulse, respectively.

Characterizing the B₁₊ field generated by the transmit coils entailed 2-D echo-planar imaging (16,17) of the head phantom (TR/TE = 3000/24.1ms, echo-spacing = 1.33ms, 1.25×1.25cm² in-plane resolution, 20×20cm² FOV, 16×16 matrix, ±7.58kHz readout bandwidth, and 5cm slice thickness) using a single-band spectral-spatial (SPSP) RF pulse (130 Hz FWHM, 868 Hz stopband) to selectively excite the central ¹³C resonance of ethylene glycol. To correct for EPI Nyquist ghost artifacts arising from phase errors, a reference scan was first acquired with phase-encoding gradients disabled. Axial and mid-sagittal slices of the head phantom were then imaged along the magnet iso-center. By acquiring the data with flip angles α=60° and 2α=120° (100 averages each), flip angle maps could be calculated according to the double angle method, with the T₁ of ethylene glycol measured as 700ms (18). Relative B₁₊ maps were obtained by normalizing each map by the mean flip angle.

Receiver sensitivity maps were obtained using a 3-D stack-of-EPI (9) variant (α=20°, TR/TE=47/21.7ms, echo-spacing=0.528ms, 1cm isotropic resolution, 32×32cm² FOV, 32×32 matrix, ±167kHz readout bandwidth, 2800 NEX, 70min.). Noise data were also acquired separately without transmit RF power and the noise covariance matrix calculated as:

$$\Psi_{ij} = \frac{1}{N} \sum_{k=1}^N n_i(k)n_j^*(k)$$

, where *N* is the number of complex data samples for all coils; *n_i(k)* is *k*th sample from element *i*; and *n_j^{*}(k)* is the complex conjugate of the *k*th sample from element *j* (19). To assess coil coupling, the noise correlation matrix (Ψ_{ij}^{corr}) was also computed as a normalized version of Ψ_{ij} (20):

$$\Psi_{ij}^{corr} = \frac{\Psi_{ij}}{\sqrt{\Psi_{ii}\Psi_{jj}}}$$

Data were prewhitened via Cholesky decomposition (21) of the noise covariance matrix (Ψ) and combined using complex weights derived from the fully-sampled data (22). Coil-combined data were summed through time and the SNR computed by dividing by the standard deviation of the noise after correcting for Rician bias (23). SNR line profiles were computed along principal imaging planes, with each point representing the mean of three adjacent voxels.

In vivo Imaging

Patient studies were approved by the IRB at UCSF and conducted with informed consent. Dynamic hyperpolarized ^{13}C data were acquired from a patient with a brain tumor for each coil configuration using 2-D multislice EPI (TR/TE=62.5/21.7ms, 3 frequencies, $\alpha_{\text{pyruvate}}/\alpha_{\text{lactate}}/\alpha_{\text{bicarbonate}}=20^\circ/30^\circ/30^\circ$, $1.5\times 1.5\text{cm}^2$ in-plane spatial resolution, eight 2cm slices, 20 timepoints, 3s temporal resolution)(9). The 8-channel exam was performed 2 months prior to the 32-channel exam, with the surface coils placed directly against the head (~15cm width). There was no change in the clinical or radiographic status of the patient between acquisitions. Transmit gains were calibrated on the ethylene glycol head phantom and an embedded 1 mL 8M ^{13}C -urea sample provided *in vivo* frequency referencing: $f_{\text{pyruvate}} = f_{\text{urea}} + 270\text{Hz}$. A 1.47g sample of $[1-^{13}\text{C}]$ pyruvate was polarized using a GE SpinLab system (5) and injected intravenously at 5mL/s, with a 5s post-injection delay prior to imaging. Noise-only EPI data were obtained as part of the protocol and utilized in post-processing. After completing the ^{13}C EPI acquisition, the patient was repositioned and a standard ^1H MR examination was performed with a 32-channel ^1H coil (Nova Medical Inc., Wilmington, MA).

After processing the EPI metabolite data as above using the pyruvate signal for coil combination, the reconstructed dynamic data was summed over time. A separate noise-only acquisition was performed following the hyperpolarized study to ensure a sufficient number of voxels to estimate the noise. SNR values were corrected for concentration, polarization, and time-to-injection, assuming a $[1-^{13}\text{C}]$ pyruvate solution state T_1 of 71s. A set of 3-D T_1 -weighted images (TR/TE/TI =6652/2448/450ms, resolution= $1.5\times 1\times 1\text{mm}^3$, 25.6-cm FOV, 256×256 matrix) from the subsequent ^1H examination were aligned by FLIRT (24) to body coil FSE images from the ^{13}C examination to enable anatomic referencing. White matter (WM) segmentation was performed on aligned T_1 -weighted images using the FSL FAST algorithm (25). The ^{13}C data voxels that contained > 60% of WM were used to compare lactate-to-pyruvate ratios from both exams.

Results

Relative B_{1+} maps for each hardware configuration are shown in Figure 2, along with associated histograms. Based on the distribution of values over the mid-sagittal section of the phantom, the birdcage displayed more uniform B_{1+} compared to the clamshell, with a fractional error of 0.06 versus 0.10 (Figure 2A,B; *top*). The field homogeneity of the birdcage (0.07, fractional error) also exceeded that of the clamshell (0.12) in the axial B_{1+} map, corresponding to the central brain (Figure 2A,B; *bottom*). Coupling characteristics for individual receive elements are presented in Supporting Information Figure S2 via noise correlation matrices (Ψ^{corr}), which showed an average off-diagonal of 0.30 and 0.24 for 8- and 32-channel receiver arrays, respectively.

Multi-plane SNR maps from the phantom are shown in Figure 3A. These display the relative sensitivities of the birdcage transceiver; 8- and 32-channel receiver arrays with matched lateral separation (19cm); and the 8-channel paddles placed directly on the phantom (16.3cm). The birdcage transceiver exhibited the most uniform profile, with extensive coverage that was comparable to the 32-channel array over relevant imaging regions.

Whereas the 32-channel array demonstrated the greatest sensitivity at the anterior/posterior of the phantom, and the region corresponding to mid-sagittal cortex, the sensitivity of the 8-channel coil was more pronounced along the lateral aspect of the brain, and decreased markedly toward the midline. Mean SNR line profiles along principle imaging planes recapitulate these sensitivity characteristics (Figure 3B–D). From right-left (R-L) profiles, the transceiver-normalized SNR at the center of the phantom was 0.97, 0.91, and 1.45 (32ch/transceiver, 8ch_{19cm}/transceiver, 8ch_{16.3cm}/transceiver), with an average of 2.08, 3.01, and 6.67 on the periphery (Fig 3B). Anterior-posterior (A-P) profiles show transceiver-normalized SNR of 2.73, 0.66, and 1.38 (32ch/transceiver, 8ch_{19cm}/transceiver, 8ch_{16.3cm}/transceiver) at the anterior aspect and 3.17, 0.67, and 0.93 at the posterior aspect of the phantom midline (Fig 3C). Inferior-superior (S-I) profiles display similar SNR advantages and extended coverage for the 32-channel array at the top of the head (Fig 3D). The percentage of total SNR relative to the transceiver for each hardware configuration within a 11-cm thick axial ROI encompassing the brain region was: 136% (8ch_{19cm}/transceiver), 175% (32ch/transceiver), and 254% (8ch_{16.3cm}/transceiver). Within this ROI, the percentage of voxels exceeding the mean SNR of the central 27 voxels from the birdcage transceiver data was: 47% (8ch_{19cm}), 69% (32ch), and 69% (8ch_{16.3cm}).

For serial scans that were performed on the same patient, the comparison was based on metabolite SNR maps that were overlaid on T₁-weighted images to show anatomical correspondence (Figure 4). Patient head width (~15cm) allowed for closer placement of 8-channel paddles. The 8-/32-channel exam parameters were: 23/22mL injected pyruvate volume, 247/254mM concentration, 41.7/33.1% polarization, and 54/53s time-to-injection. Parameter-normalized, temporally-summed pyruvate and lactate SNR data (SNR >5) are displayed for each hardware configuration in Figure 4A,B; SNR comparisons are presented in Supporting Information Figure S3. The ratios of mean slice SNR, $[\text{SNR}_{\text{mean},8\text{-channel}}/\text{SNR}_{\text{mean},32\text{-channel}}]_{\text{pyruvate}}$ and $[\text{SNR}_{\text{mean},8\text{-channel}}/\text{SNR}_{\text{mean},32\text{-channel}}]_{\text{lactate}}$, showed an advantage for the 32-channel and 8-channel arrays at the top and center of the brain, respectively: 0.51,0.58; 0.99,1.02; 1.59,1.66; and 1.83,2.00 (superior-to-inferior slices). The improved SNR of the 8-channel hardware at the center of the brain was also seen in the bicarbonate SNR map (Figure 4C). Lactate-to-pyruvate ratios in white matter voxels (Supporting Information Figure S3) were comparable across hardware platforms: 0.45 ± 0.12 (8-channel) versus 0.43 ± 0.14 (32-channel).

Discussion

This study compared the SNR performance of 8- versus 32-channel hardware configurations for ¹³C hyperpolarized imaging of the brain using phantom and patient experiments. By characterizing the utility of these particular implementations in practice, it was possible to elucidate inherent trade-offs that influence their application, and thusly inform efforts towards future coil design.

Quantitative assessment of the B₁₊ field produced by each transmit coil ensured that the receiver arrays were evaluated on a fair basis. As expected, the quadrature birdcage coil demonstrated the most uniform B₁₊ field within the brain, aided by its 16-rung design. Although performing adequately, the clamshell transmit coil showed increased B₁₊

inhomogeneity, consistent with a Helmholtz pair (26), which is problematic for hyperpolarized studies with non-renewable magnetization. Additionally, the increased B_1+ requirements for carbon applications may impose limitations on short duration and adiabatic pulses, highlighting the power inefficiency associated with linearly polarized fields (27). With regard to receiver performance, both the 8- and 32-channel arrays showed similar coupling from noise-only data, but some of the elements in the 32-channel array may have had worse noise characteristics on account of their larger size ($\sim 79\text{cm}^2$ versus 50cm^2).

Based on the distinct reception profiles exhibited by the 8- and 32-channel arrays in phantom experiments relative to the birdcage in transceiver mode, each may be viewed as providing advantages for imaging specific brain anatomy. Whereas the 8-channel array displayed the most sensitivity along the lateral aspects (temporal/parietal lobes), the 32-channel array was found to be more sensitive in the region corresponding to the frontal and occipital lobes along the apical cortex. Under the condition of matched lateral separation, the total SNR of the 32-channel array was 29% greater than that of the 8-channel array and 75% greater than that of the birdcage transceiver in the region encompassing the brain. Although the 32-channel array demonstrated slightly lower SNR compared to the birdcage transceiver near the center of the brain region, this was compensated by higher SNR in 69% of the covered volume, including significant gains in the abovementioned anatomy.

In vivo experiments corroborated results obtained from the phantom and provided comparative examples of multi-metabolite EPI data on each hardware platform. In addition to confirming the superior uniformity of the 32-channel coil-combined reception profile, these data showed the same relative coil sensitivities observed in the phantom. In this case, the small head size of the patient (~ 15 cm across) allowed the paddle coils to be placed closer together and the 8-channel array outperformed the head array coil at the center of the brain, to a greater extent than expected based on phantom experiments having similar hardware positioning. Given the nature of hyperpolarized experiments, the large number of factors that influence the magnitude of the observed signal complicate direct comparisons with phantom data. The fact that the white matter lactate-to-pyruvate ratios were conserved across patient exams is encouraging and indicates that these two distinct coil configurations provide comparable results.

Because of the range of trade-offs demonstrated, the appropriate choice of hardware for *in vivo* ^{13}C hyperpolarized imaging of brain would depend upon the specific anatomy under investigation and type of study. In the case of the 32-channel head array coil, there is a strong argument for it being clinically translatable, based on the ease of positioning patients and uniformity of the coil-combined profile. Moreover, the greater receiver count enhances the capacity for acceleration via parallel imaging. Undesirable aspects of this coil relate to the larger coil size and rigid housing that is suboptimal for smaller heads. Despite its nonuniform profile, the 8-channel coil confers modularity, which allows for tailored placement on the region of interest, and has demonstrable SNR advantages that may benefit pediatric and brainstem applications. Since hyperpolarized ^{13}C brain imaging falls within an SNR/resolution-limited regime, the optimal future design is most likely a multi-channel head array that conforms more closely to the average head size.

Conclusion

With matched separation between lateral receiver elements, the 8- and 32-channel hardware configurations demonstrated similar SNR performance at the center of the brain, however the 32-channel array/birdcage transmitter provided greater total SNR and extent of coverage, along with a more uniform coil-combined profile. The 8-channel coil/clamshell transmitter may offer SNR benefits for smaller heads and brainstem applications because of their modularity.

Supplementary Material

Refer to Web version on PubMed Central for supplementary material.

Acknowledgements

This work was supported by NIH Grants R01 CA127612, P01 CA118816 and P41 EB0341598. The recipe for adjusting conductivity in the ethylene glycol phantom to approximate physiological loads was provided courtesy of the Center for Hyperpolarization in Magnetic Resonance, Technical University of Denmark.

References

1. Ardenkjaer-Larsen JH, Fridlund B, Gram A, Hansson G, Hansson L, Lerche MH, Servin R, Thaning M, Golman K. Increase in signal-to-noise ratio of > 10,000 times in liquid-state NMR. *Proc Natl Acad Sci USA*. 2003; 100(18):10158–63 [PubMed: 12930897]
2. Nelson SJ, Kurhanewicz J, Vigneron DB, Larson PEZ, Harzstark AL, Ferrone M, van Criekinge M, Chang JW, Bok R, Park I, Reed G, Carvajal L, Small EJ, Munster P, Weinberg VK, Ardenkjaer-Larsen JH, Chen AP, Hurd RE, Odegardstuen LI, Robb FJ, Tropp J, Murray JA. Metabolic imaging of patients with prostate cancer using hyperpolarized [1-¹³C]pyruvate. *Sci Transl Med*. 2013; 5(198): 198ra108
3. Cunningham CH, Lau JYC, Chen AP, Geraghty BJ, Perks WJ, Roifman I, Wright GA, and Connelly KA. Hyperpolarized ¹³C Metabolic MRI of the Human Heart: initial experience. *Circ Res*. 2016; 119(11): 1177–1182 [PubMed: 27635086]
4. Grist JT, McLean MA, Riemer F, Schulte RF, Deen SS, Zaccagna F, et al. Quantifying normal human brain metabolism using hyperpolarized [1-¹³C]pyruvate and magnetic resonance imaging. *NeuroImage* 2019; 189: 171–179 [PubMed: 30639333]
5. Park I, Larson PEZ, Gordon JW, Carvajal L, Chen HY, Bok R, Van Criekinge M, Ferrone M, Slater JB, Xu D, Kurhanewicz J, Vigneron DB, Chang S, Nelson SJ. Development of methods and feasibility of using hyperpolarized carbon-13 imaging data for evaluating brain metabolism in patient studies. *Magn Reson Med*. 2018; 80(3):864–873 [PubMed: 29322616]
6. Miloushev VZ, Granlund KL, Boltyanskiy R, Lyashchenko SK, DeAngelis LM, Mellinghoff IK, Brennan CW, Tabar V, Yang TJ, Holodny AI, Sosa RE, Guo YW, Chen AP, Tropp J, Robb F, Keshari KR. Metabolic imaging of the human brain with hyperpolarized ¹³C pyruvate demonstrates ¹³C lactate production in brain tumor patients. *Cancer Res*. 2018; 78(14): 3755–3760 [PubMed: 29769199]
7. Tropp J, Calderon P, Carvajal L, Robb F, Larson PEZ, Shin P, Vigneron DVB, Nelson SJ. A carbon receive array of 8 elements, interoperable with proton scanning, for human temporal lobe. *Proc. Intl. Soc. Mag. Reson. Med* 2012, abstract#2658
8. Wiggins GC, Triantafyllou C, Potthast A, Reykowski A, Nittka M, Wald LL, 32-channel 3 Tesla receive-only phased-array head coil with soccer-ball element geometry. *Magn Reson Med*. 2006; 56: 216–223 [PubMed: 16767762]
9. Hayes CE, Hattes N, Roemer PB, Volume imaging with MR phased arrays. *Magn Reson Med*. 1991; 18: 309–319 [PubMed: 2046514]

10. Sodickson DK, Manning WJ. Simultaneous acquisition of spatial harmonics (SMASH): fast imaging with radiofrequency coil arrays. *Magn Reson Med*. 1997; 38: 591–603 [PubMed: 9324327]
11. Sodickson DK, McKenzie CA. A generalized approach to parallel magnetic resonance imaging. *Medical Physics* 2001; 28: 1629–1643 [PubMed: 11548932]
12. Stehling MK, Turner R, Mansfield P. Echo-planar imaging: magnetic resonance imaging in a fraction of a second. *Science* 1991; 254: 43–50 [PubMed: 1925560]
13. Tropp J, Lupo JM, Chen A, Calderon P, McCune D, Grafendorfer T, Ozturk-Isik E, Larson PE, Hu S, Yen YF, Robb F, Bok R, Schulte R, Xu D, Hurd R, Vigneron D, Nelson S. Multi-channel metabolic imaging, with SENSE reconstruction, of hyperpolarized [1-(13)C]pyruvate in a live rat at 3.0 tesla on a clinical MR scanner. *J Magn Reson*. 2011; 208(1): 171–7 [PubMed: 21130012]
14. Mareyam A, Carvajal L, Xu D, Gordon JW, Park I, Vigneron DB, Nelson SJ, Stockmann JP, Keil B, and Wald LL. 31-Channel brain array for hyperpolarized 13C imaging at 3T. *Proc. Intl. Soc. Mag. Reson. Med* 2017, abstract#1225
15. Tropp J, Sugiura S. A dual-tuned probe and multiband receiver front end for X-nucleus spectroscopy with proton scout imaging in vivo. *Magn Reson Med*. 1989; 11:405–412. [PubMed: 2550721]
16. Gordon JW, Vigneron DB, and Larson PEZ. Development of a symmetric echo planar imaging framework for clinical translation of rapid dynamic hyperpolarized ¹³C imaging. *Magn Reson Med*. 2017; 77: 826–832 [PubMed: 26898849]
17. Autry AW, Gordon JW, Carvajal L, Park I, Mammoli D, Chen H, Chang S, Li Y, Xu D, Vigneron DB, and Nelson SJ. Comparison between 8- and 32-channel phased-array receive coils for in vivo hyperpolarized C-13 brain imaging. *Proc. Intl. Soc. Mag. Reson. Med* 2018, abstract#3565
18. Stollberger R, Wach P. Imaging of the active B1 field in vivo. *Magn Reson Med*. 1996; 35: 246–251 [PubMed: 8622590]
19. Kellerman P, McVeigh ER. Image reconstruction in SNR units: a general method for SNR measurement. *Magn Reson Med*. 2005; 54(6): 1439–47. [PubMed: 16261576]
20. Ohliger MA, Sodickson DK. An introduction to coil array design for parallel MRI. *NMR Biomed*. 2006; 19(3): 300–315 [PubMed: 16705631]
21. Pruessmann KP, Wiegner M, Boernert P, Boesiger P. Advances in sensitivity encoding with arbitrary k-space trajectories. *Magn Reson Med*. 2001;46:638–651 [PubMed: 11590639]
22. McKenzie CA, Yeh EN, Ohliger MA, Price MD, Sodickson DK. Self-calibrating parallel imaging with automatic coil sensitivity extraction. *Magn Reson Med*. 2002; 47(3): 529–38 [PubMed: 11870840]
23. Gudbjartsson H, Patz S. The Rician distribution of noisy MRI data. *Magn Reson Med*. 1995; 34: 910–914 [PubMed: 8598820]
24. Jenkinson M, Smith SM. A global optimisation method for robust affine registration of brain images. *Medical Image Analysis*. 2001; 5(2): 143–156 [PubMed: 11516708]
25. Zhang Y, Brady M, Smith S. Segmentation of brain MR images through a hidden random field model and the expectation-maximization algorithm, *IEEE Trans Med Imag*. 2001; 20(1): 45–57
26. Hurtado-Velasco R, Gonzalez-Llorente J. Simulation of the magnetic field generated by square shape Helmholtz coils. *Applied Mathematical Modeling*, 2016; 40:9835–9847
27. Bernstein M, King KF, Zhou XJ. *Handbook of MRI Pulse Sequences*. New York: Elsevier, New York; 2004 p. 69

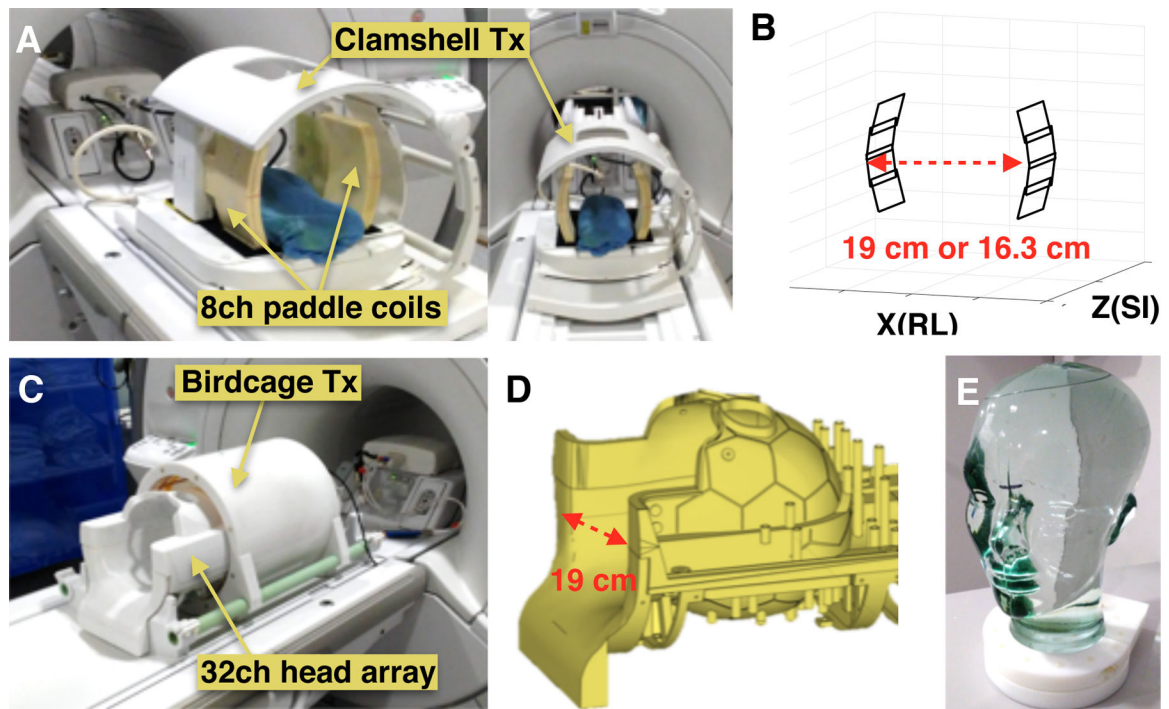


Figure 1. Hardware setup showing images of the 8-channel bilateral surface coils and clamshell transmitter (A), along with a schematic of individual receiver elements (5 cm × 10 cm each) in the phased array (B). The schematic depicts the two experimental phantom setups explored, where the surface coils are either separated by 19 cm (8ch_{19cm}) to match the 32-channel housing or by 16.3 cm (8ch_{16.3cm}) when placed directly against the phantom. Images of the 32-channel head array coil and birdcage transmitter (C) are also shown with a schematic of the 32-channel housing that details relative receiver element arrangements (D). The ethylene glycol head phantom has dimensions of 15 cm right-left, 18 cm anterior-posterior and 22 cm superior-inferior (E).

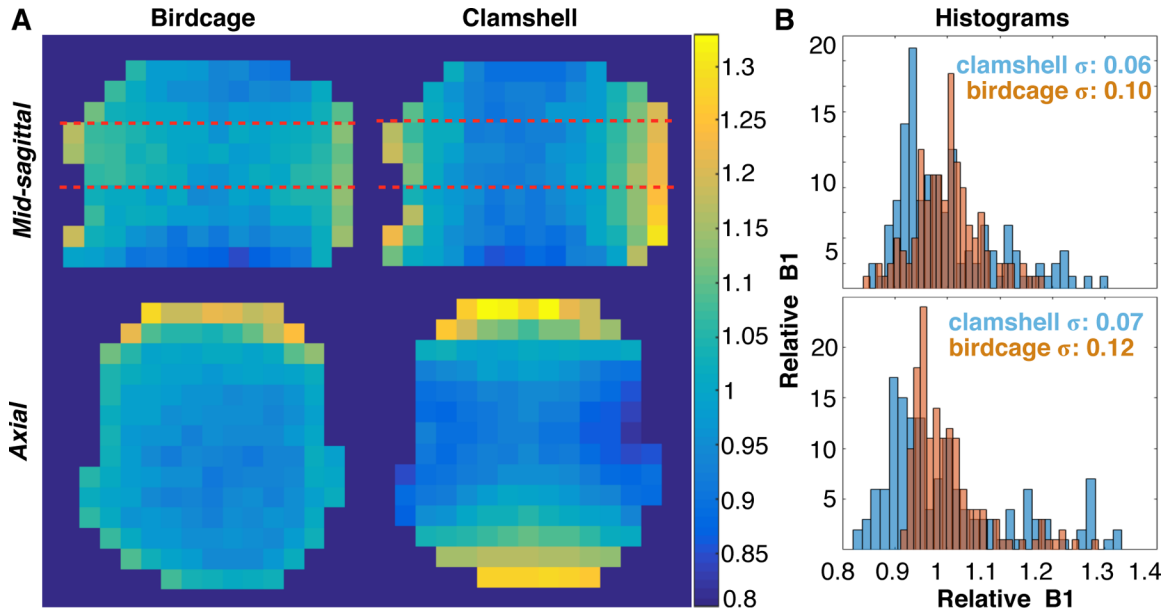


Figure 2. B_{1+} characterization.

Relative B_{1+} maps for the birdcage and clamshell transmitters obtained from 5 cm mid-sagittal and axial slices through an ethylene glycol head phantom (A). Red dashed lines delimit the location of axial slices in the region corresponding to the center of the brain.

Associated histograms show the relative transmitter B_{1+} distributions for each imaging plane (B).

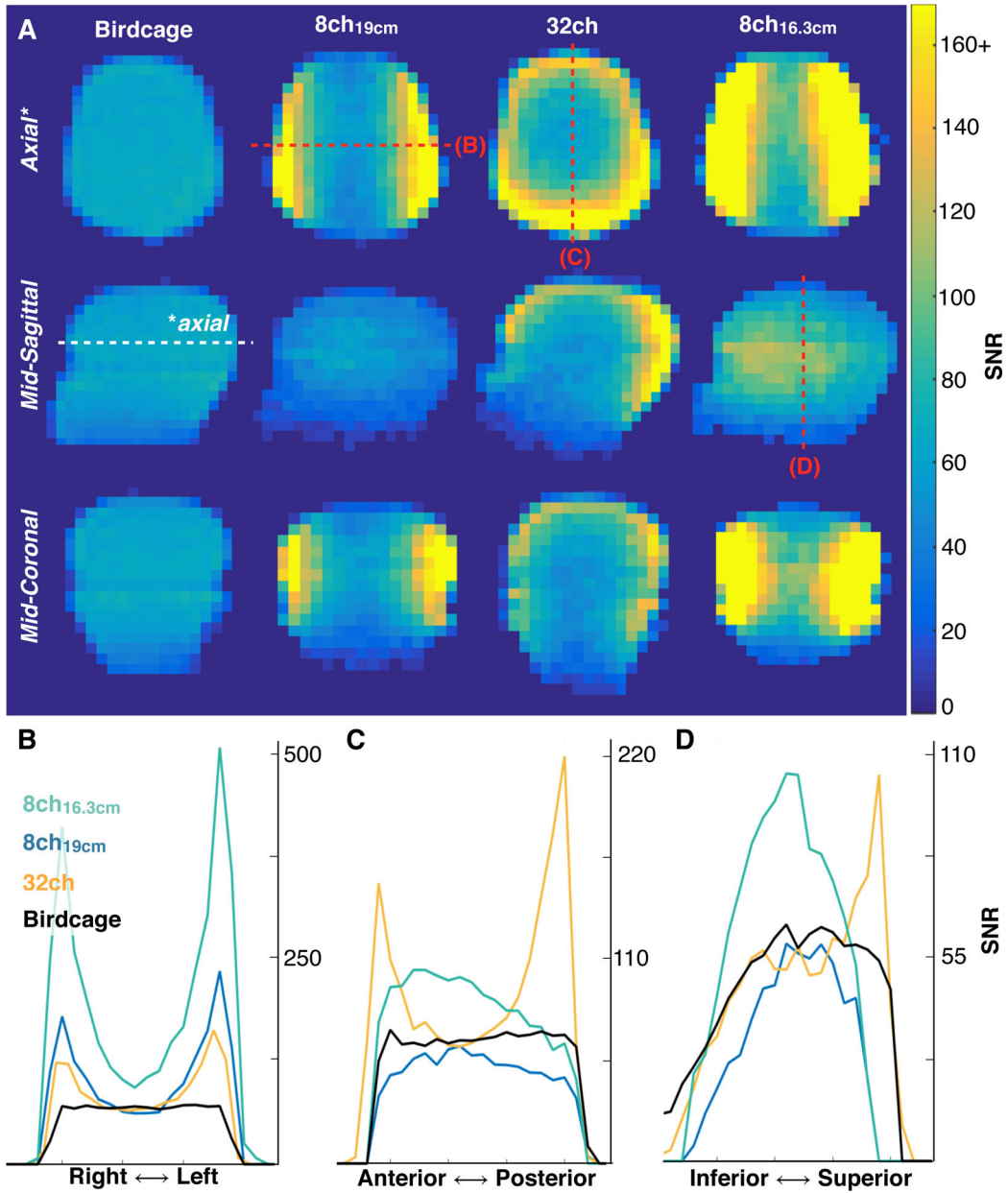


Figure 3. Phantom SNR.

SNR data with 1 cm³ spatial resolution derived from 3-D echo-planar imaging of an ethylene glycol head phantom using: the birdcage transceiver; the 8-channel paddle coils separated by 19 cm (8ch_{19cm}) to match the 32-channel housing; the 32-channel array; and the 8-channel paddle coils placed directly on the phantom, separated by 16.3 cm (8ch_{16.3cm}) (A). Axial (white dashed line), mid-coronal, and mid-sagittal planes are shown, along with corresponding right-left (B), anterior-posterior (C), and superior-inferior (D) SNR line profiles, referenced by red dashed lines on (A); each profile point represents the mean of 3 adjacent voxels.

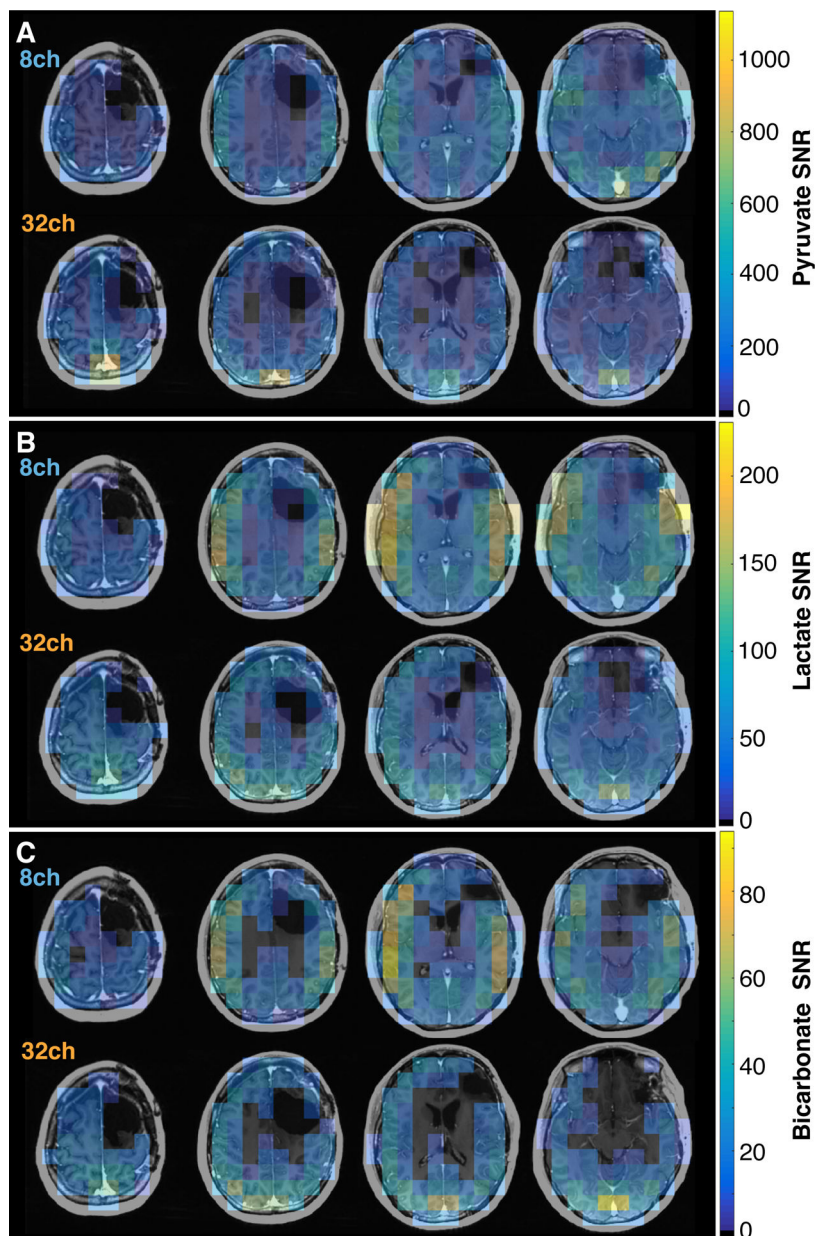


Figure 4. *In vivo* hyperpolarized data.

Hyperpolarized 2-D multi-slice EPI data having 4.5 cm³ spatial resolution acquired from a patient with a brain tumor using the 8- and 32-channel hardware configurations (8-channel paddles placed directly against the 15 cm head). Temporally-summed, parameter-normalized SNR>5 data for [1-¹³C]pyruvate (A) and [1-¹³C]lactate (B) are shown overlaid on ¹H T₁ post-contrast images. Ratios of mean slice SNR, [SNR_{mean,8-channel}/SNR_{mean,32-channel}]pyruvate and [SNR_{mean,8-channel}/SNR_{mean,32-channel}]lactate, were: 0.51,0.58; 0.99,1.02; 1.59,1.66; and 1.83,2.00 (superior-to-inferior slices). SNR>5 bicarbonate data depicts contrasting hardware sensitivity in the center of the brain (C).

Table 1.

Hardware specifications.

	8-channel configuration	32-channel configuration
RF Transmitter	Clamshell Capacitively-coupled Helmholtz pair (square loops ~30.5×30.5 cm ²)	16-rung low-pass birdcage (30.5 cm diameter, 32 cm rung length)
Receiver elements	2 paddle coils, 4 elements each (5 cm × 10 cm)	Hexagonal/pentagonal soccer ball geometry: 16 elements on top; 16 on bottom (8–10 cm diameter) $Q_{UL}/Q_L = 250/90$
		Return loss (S_{11}) < -17dB
Receiver decoupling	Overlapped to minimize mutual inductance Pre-amp decoupling for next-to-nearest neighbor Transmission loss (S_{21}) < -17dB for nearest neighbor	
Detuning & blocks	Active detuning for carbon >30dB with passive blocking for proton	
Preamps	28 dB gain	

Author Manuscript

Author Manuscript

Author Manuscript

Author Manuscript